



HAL
open science

A spectral projection method for the simulation of complex three-dimensional rotating flows

Isabelle Raspo, Sandrine Hugues, Eric Serre, Anthony Randriamampianina,
Patrick Bontoux

► **To cite this version:**

Isabelle Raspo, Sandrine Hugues, Eric Serre, Anthony Randriamampianina, Patrick Bontoux. A spectral projection method for the simulation of complex three-dimensional rotating flows. *Computers and Fluids*, 2002, 31 (4-7), pp.745-767. 10.1016/S0045-7930(01)00070-6 . hal-00833836

HAL Id: hal-00833836

<https://hal.science/hal-00833836>

Submitted on 16 Jan 2024

HAL is a multi-disciplinary open access archive for the deposit and dissemination of scientific research documents, whether they are published or not. The documents may come from teaching and research institutions in France or abroad, or from public or private research centers.

L'archive ouverte pluridisciplinaire **HAL**, est destinée au dépôt et à la diffusion de documents scientifiques de niveau recherche, publiés ou non, émanant des établissements d'enseignement et de recherche français ou étrangers, des laboratoires publics ou privés.

A spectral projection method for the simulation of complex three-dimensional rotating flows

Isabelle Raspo^{a,*}, Sandrine Hugues^a, Eric Serre^a,
Anthony Randriamampianinab, Patrick Bontoux^a

^aLMSNM, FRE 2405 CNRS, La Jetée, Technopôle de Château-Gombert, 38 rue Frédéric Joliot Curie,
13451 Marseille, France

^bIRPHE, UMR 6594 CNRS, Technopôle de Château-Gombert, 49 rue Frédéric Joliot Curie, 13384 Marseille, France

In this paper, we present an efficient projection method to solve the three-dimensional time-dependent incompressible Navier–Stokes equations in primitive variables formulation using spectral approximations. This method is based on a modification of the algorithm proposed by Goda [J. Comp. Phys. 30 (1979) 76]. It brings an improvement by introducing a preliminary step for the pressure in order to allow a temporal evolution of the normal pressure gradient at the boundaries. Its efficiency is brought to the fore by comparison with the Goda’s algorithm. The modified projection method is then applied to the simulation of complex three-dimensional flows in rotating cavities, involving either a throughflow or a differential rotation.

Keywords: Projection methods; Spectral approximations; Instabilities; Rotating systems

1. Introduction

When solving the incompressible Navier–Stokes equations with the primitive variables, the main difficulties arise from the lack of an evolution equation for the pressure, which only appears through its gradient in the momentum equations, and from the treatment of the incompressibility constraint. For incompressible flows, the pressure is not a thermodynamic variable since it does not satisfy a state equation. From a mathematical point of view, it is a kind of Lagrange

* Corresponding author. Tel.: +33-4-9111-8549; fax: +33-4-9111-8502.
E-mail address: isabel@l3m.univ-mrs.fr (I. Raspo).

multiplier ensuring that the velocity field is divergence free at each time step. This leads to a strong coupling between the pressure and the velocity field. Several techniques were proposed in order to treat this coupling. The way chosen in the present paper is to use projection methods. These methods, also called fractional steps or splitting methods, consist in solving the momentum and the continuity equations in two main steps. First, a predicted velocity field, which is not divergence free, is computed from the discretized momentum equations. In a second step, this velocity field is corrected in order to fulfil the incompressibility constraint. This latter step is generally performed by solving a Poisson equation for the pressure, which is derived from the momentum equations by requiring incompressibility. However, it can also be treated as a Darcy problem [2,14].

The first projection method was developed by Chorin [4] and Temam [33] for finite difference approximations. The predicted velocity field was computed by only taking into account the convective and diffusive terms in the momentum equations. The pressure field at the current time step, ensuring that the velocity field is divergence free, was then obtained in the projection step by solving a Poisson equation with the predicted velocity divergence as source term. Homogeneous Neumann boundary conditions were used for the pressure. This scheme was first order accurate in time. However, due to the implicit character of the scheme, the boundary conditions for the pressure induce a loss of accuracy in the final solution. This lack of accuracy was corrected by Fortin et al. [7] by using an explicit scheme. In the framework of finite element approximations, Goda [9] proposed an improvement of the method by taking into account the pressure gradient at the previous time step in the computation of the predicted velocity field. The projection step was then performed by solving a Poisson problem for an intermediate variable φ which is in fact the pressure difference between the current and the previous time steps. This improved algorithm was used later with finite difference approximations and a Crank–Nicolson scheme for time discretization by Van Kan [35] who showed that the method keeps the accuracy order of the temporal scheme. However, the main weakness of this algorithm lies in the fact that the homogeneous Neumann boundary condition imposed for the intermediate variable φ constrains the normal pressure gradient at the boundary to keep its initial value.

More recently, Botella [2] used a similar projection method with a third order temporal scheme and a collocation–Chebyshev approximation. However, in his approach, the projection step is treated as a Darcy problem, which does not require boundary conditions for the pressure. In order to get rid of the pressure spurious modes, Botella used a $P_N \times P_{N-2}$ discretization, i.e. the pressure is approximated with polynomials of degree two less than those used for the velocity field. A similar projection scheme was also used by Heinrichs [14] with a $P_N \times P_N$ approximation for the solution of the unsteady Stokes equations. He compared his method with the classical one (i.e. when the projection step is solved through a Poisson equation for the pressure) in the case of a steady exact solution. The results showed that the same space accuracy is obtained with the two methods provided that the Poisson problem is solved with the improved Neumann boundary condition proposed by Karniadakis et al. [18].

Another projection algorithm, based on the Chorin–Temam method, was also proposed for finite difference approximations by Kim and Moin [19]. They introduced the gradient of an intermediate variable Φ in the boundary condition of the predicted velocity field. The equations are solved using this new variable Φ instead of the pressure. This method was also used in association

with a Chebyshev–Tau approximation by Shen [30] to solve two-dimensional incompressible Navier–Stokes equations.

However, all the projection schemes described above induce a slip velocity on the boundary since the tangential boundary conditions are not prescribed in the projection step [32].

More complex projection algorithms were also proposed in the literature. In the framework of spectral element discretizations, Karniadakis et al. [18] developed a method in which the Navier–Stokes equations are solved over three steps. A first velocity field, which does not fulfil the incompressibility constraint, is computed explicitly by taking into account only the non-linear terms. Then, the projection step is performed by solving the pressure Poisson equation with the divergence of this predicted velocity as a source term. The final divergence free velocity field is computed implicitly during a third step by taking into account the diffusive terms and the pressure gradient at the current time step. Karniadakis et al. also proposed a high order pressure boundary condition for the projection step. Neumann conditions are obtained by projecting the discretized momentum equations normally to the boundary. The viscous linear terms are written in terms of a solenoidal part, approximated by an explicit scheme, and an irrotational part, approximated by an implicit scheme. Such a decomposition of the viscous terms was previously proposed in association with a reflection technique by Pracht [22]. The pressure boundary condition used by Karniadakis et al. avoids the propagation and the accumulation of time differencing errors and allows the pressure compatibility condition to be automatically satisfied. A similar method was used later by Batoul et al. [1] with a collocation–Chebyshev approximation. It can be noted that the algorithm proposed by Karniadakis et al. is in fact a projection method in which the diffusion and the projection steps are inverted. Thus, the velocity field satisfies both the normal and the tangential boundary conditions but it does not fulfil the incompressibility constraint in a boundary layer of thickness $(\nu \delta t)^{1/2}$.

In this paper, an efficient projection method is proposed to solve the three-dimensional time-dependent incompressible Navier–Stokes equations using a collocation–Chebyshev–Fourier approximation. This method is a modification of the projection algorithm developed by Goda. The accuracy of projection methods depends strongly on the boundary conditions prescribed for the pressure. Detailed studies on these pressure boundary conditions were carried out by several authors [12,21]. The improvement brought by the algorithm proposed here results from a special treatment of the pressure boundary conditions. More precisely, a preliminary step is introduced in which an intermediate pressure field is computed from the Navier–Stokes equations [16,17]. This preliminary pressure, which is taken into account in the computation of the predicted velocity field, allows the normal pressure gradient at the boundary to vary with time in order to recover the one of the solution of the Navier–Stokes equations. Moreover, it involves a better achievement of the incompressibility constraint on the boundary.

The first section is devoted to the description of the mathematical modelling and the numerical approximation. Then, the Goda’s projection method (GPM) and the modified one are presented. In Section 4, the space and the time accuracies are checked on exact analytical solutions. In particular, we show the inability of the GPM to treat correctly solutions with time-dependent pressure gradients on the boundary and that the introduction of the preliminary pressure allows to recover a high accuracy for such solutions. The final section is devoted to the application of the modified algorithm to the simulation of three-dimensional rotating cavities with and without throughflow.

2. Mathematical modelling and numerical approximation

2.1. Mathematical modelling

We consider the three-dimensional time-dependent and incompressible flows of a Newtonian fluid contained in an annular cavity bounded by two co-axial cylinders of respective radii a and b ($b > a$) and two disks spaced by a distance $2L$. Depending on the problem, one or several walls of the system rotates around the axis ($0z$) with an angular velocity Ω . The flow is governed by the three-dimensional Navier–Stokes equations considered in the primitive variables formulation:

$$\begin{cases} \frac{\partial \mathbf{V}}{\partial t} + \mathbf{V} \cdot \nabla \mathbf{V} = -\nabla p + \nu \Delta \mathbf{V} + \mathbf{F} & \text{in } D & (1) \\ \mathbf{V} = \mathbf{W} & \text{on } \Gamma = \partial D & (2) \\ \nabla \cdot \mathbf{V} = 0 & \text{in } \bar{D} = D \cup \Gamma & (3) \end{cases}$$

where \mathbf{V} is the velocity of components (u, v, w) respectively in radial r , azimuthal θ and axial z directions, p is the pressure, ν the kinematic viscosity, \mathbf{F} represents body forces and Δ is the Laplacian operator written for cylindrical coordinates:

$$(\Delta \mathbf{V})_r = \nabla^2 u - \frac{u}{r^2} - \frac{2}{r^2} \frac{\partial v}{\partial \theta}, \quad (\Delta \mathbf{V})_\theta = \nabla^2 v - \frac{v}{r^2} + \frac{2}{r^2} \frac{\partial u}{\partial \theta}, \quad (\Delta \mathbf{V})_z = \nabla^2 w$$

with

$$\nabla^2 = \frac{\partial^2}{\partial r^2} + \frac{1}{r} \frac{\partial}{\partial r} + \frac{1}{r^2} \frac{\partial^2}{\partial \theta^2} + \frac{\partial^2}{\partial z^2}$$

Eqs. (1)–(3) are completed by specific initial conditions for the velocity:

$$\mathbf{V} = \mathbf{V}_0 \text{ with } \nabla \cdot \mathbf{V}_0 = 0 \text{ in } \bar{D} \quad (4)$$

2.2. Time discretization and space approximation

The Navier–Stokes equations are discretized in time by using the second order semi-implicit scheme proposed by Vanel et al. [34], which consists of a fully implicit discretization of the diffusive terms with an Adams–Bashforth evaluation of the convective terms. The resulting discretized equations write:

$$\begin{cases} \frac{3\mathbf{V}^{n+1} - 4\mathbf{V}^n + \mathbf{V}^{n-1}}{2\delta t} + 2(\mathbf{V} \cdot \nabla \mathbf{V})^n - (\mathbf{V} \cdot \nabla \mathbf{V})^{n-1} = -\nabla p^{n+1} + \nu \Delta \mathbf{V}^{n+1} + \mathbf{F}^{n+1} & \text{in } D & (5) \\ \mathbf{V}^{n+1} = \mathbf{W}^{n+1} & \text{on } \Gamma & (6) \\ \nabla \cdot \mathbf{V}^{n+1} = 0 & \text{in } \bar{D} & (7) \end{cases}$$

with δt the time step.

Due to the cylindrical configuration, the solution (\mathbf{V}, p) of the above equations is 2π —periodic in the azimuthal direction. Thus, the space approximation in this direction is done using a

Fourier–Galerkin method. We note K the cut-off frequency of the Fourier series. On the other hand, in the radial and axial directions, as boundary layers develop in the meridian plane, a collocation–Chebyshev approximation is used. First, a coordinate transformation $(r, z) \rightarrow (Y, Z)$ is performed in order to change each meridian plane (r, z) into the square domain $[-1, +1] \times [-1, +1]$, in which the Chebyshev polynomials are defined. Then, for each Fourier mode, the solution (\mathbf{V}, p) is approximated by Chebyshev polynomials of degree at most equal to N in the radial direction and to M in the axial direction. The approximation Φ_{KNM} , for $\Phi = u, v, w, p$, is computed at each triplet (Y_i, θ_q, Z_j) , where $Y_i, i = 0, \dots, N$, and $Z_j, j = 0, \dots, M$, are the Gauss–Lobatto collocation points and θ_q are defined by $\theta_q = 2\pi q/K, q = 0, \dots, K - 1$.

For the computation of the non-linear terms, the derivatives in each space direction are calculated in the spectral space and the products are performed in the physical one [10]. A FFT algorithm is used to connect the spectral and physical spaces. On the other hand, for the diffusive term (which appears in the implicit part of Eq. (5)), we use the spectral differentiation matrices.

Finally, all the resulting Helmholtz and Poisson problems are solved using a full diagonalization technique for each Fourier mode. The details of the three-dimensional solver used are described in Ref. [23].

3. Projection methods

The first method that we expose below was initially proposed by Goda [9] for finite element approximations. We applied it later to spectral approximations for the computation of axisymmetric and three-dimensional rotating flows [23]. The second method brings an improvement to the basic algorithm by introducing at each time step a preliminary step for the pressure which allows a correct temporal evolution of the normal pressure gradient at the boundary [16,17].

3.1. The Goda’s projection method (GPM)

Eqs. (5)–(7) constitute a Stokes type problem coupling the velocity components u, v, w and the pressure p . The basic idea of the projection method is to compute the solution in two steps.

- *Prediction step*

First, a predicted velocity field \mathbf{V}^* is computed implicitly from Eq. (5) in which the pressure gradient at the current time step $t_{n+1} = (n + 1)\delta t$ is replaced by the one at the previous time step $t_n = n\delta t$:

$$\begin{cases} \frac{3\mathbf{V}^* - 4\mathbf{V}^n + \mathbf{V}^{n-1}}{2\delta t} + 2(\mathbf{V} \cdot \nabla \mathbf{V})^n - (\mathbf{V} \cdot \nabla \mathbf{V})^{n-1} = -\nabla p^n + \nu \Delta \mathbf{V}^* + \mathbf{F}^{n+1} & \text{in } D \\ \mathbf{V}^* = \mathbf{W}^{n+1} & \text{on } \Gamma \end{cases} \quad (8)$$

- *Projection step*

The velocity field \mathbf{V}^* is then corrected by taking into account the pressure gradient at t_{n+1} in order to satisfy the incompressibility constraint:

$$\begin{cases} \frac{3}{2\delta t}(\mathbf{V}^{n+1} - \mathbf{V}^*) = -\nabla(p^{n+1} - p^n) & \text{in } \bar{D} \\ \mathbf{V}^{n+1} \cdot \mathbf{n} = \mathbf{W}^{n+1} \cdot \mathbf{n} & \text{on } \Gamma \\ \nabla \cdot \mathbf{V}^{n+1} = 0 & \text{in } D \end{cases} \quad (10)$$

$$\mathbf{V}^{n+1} \cdot \mathbf{n} = \mathbf{W}^{n+1} \cdot \mathbf{n} \quad \text{on } \Gamma \quad (11)$$

$$\nabla \cdot \mathbf{V}^{n+1} = 0 \quad \text{in } D \quad (12)$$

with \mathbf{n} the normal to the boundary.

This step is performed by computing an intermediate variable $\varphi = 2\delta t(p^{n+1} - p^n)/3$ through a Poisson problem. A Poisson equation is derived from Eq. (10) by prescribing the continuity condition (12), and Neumann boundary conditions are obtained by projecting Eq. (10) in the normal direction to the boundary. The Poisson problem to solve is therefore:

$$\begin{cases} \nabla^2 \varphi = \nabla \cdot \mathbf{V}^* & \text{in } D \\ \frac{\partial \varphi}{\partial n} = 0 & \text{on } \Gamma \end{cases} \quad (13)$$

$$\frac{\partial \varphi}{\partial n} = 0 \quad \text{on } \Gamma \quad (14)$$

with $\partial/\partial n$ the normal derivative.

The final velocity and pressure fields are then computed from the formulas:

$$\begin{cases} \mathbf{V}^{n+1} = \mathbf{V}^* - \nabla \varphi \\ p^{n+1} = p^n + \frac{3}{2\delta t} \varphi \end{cases} \quad \text{in } \bar{D} \quad (15)$$

- *Computation of the initial pressure*

The initial pressure p_0 is computed from the Poisson equation with the Neumann boundary condition obtained from the momentum equation at $t = 0$.

It must be noted that, since the temporal scheme used involves three time levels, the initialization requires a special treatment. So, at the first time step, i.e. for $n = 0$, we impose $\Phi^{-1} = \Phi_0$, for $\Phi = u, v, w$.

- *Remarks*

The velocity field \mathbf{V}^{n+1} computed by Eq. (15) is divergence free inside the computational domain D . However, it does not fulfil exactly the incompressibility constraint on the boundary, since Eq. (13) ensuring this condition is solved only inside the domain.

On the other hand, only the boundary conditions for the normal velocity component are prescribed in the projection step. This induces a slip velocity on the boundary. This slip velocity is defined by $V_s = \boldsymbol{\tau}(\mathbf{V}^{n+1} - \mathbf{W}^{n+1})$, with $\boldsymbol{\tau}$ the tangent to the boundary, in a two-dimensional domain and by $\mathbf{V}_s = \mathbf{n} \times ((\mathbf{V}^{n+1} - \mathbf{W}^{n+1}) \times \mathbf{n})$ in a three-dimensional one. According to Eq. (15), we have in the two-dimensional case:

$$V_s = -\boldsymbol{\tau} \cdot \nabla \varphi = -\frac{2\delta t}{3} \frac{\partial}{\partial \boldsymbol{\tau}} (p^{n+1} - p^n) \quad (16)$$

which implies that the slip velocity V_s is $O(\delta t^2)$.

Finally, it must be noted that, due to the homogeneous Neumann boundary condition prescribed for φ , the normal pressure gradient at the boundary is held at its initial value during the time integration.

3.2. The modified projection method (MPM)

A detailed description of the algorithm is given in Ref. [17] for the solution of the 2D Navier–Stokes equations with a Chebyshev–collocation approximation. We present here its extension to three-dimensional configurations (see also Ref. [16]). The aim of this method is to allow a correct temporal evolution of the normal pressure gradient at the boundary in order to follow the one of the solution of the Navier–Stokes equations. The improvement is performed by computing a preliminary pressure consistent with a divergence free velocity field.

- *Preliminary step*

A preliminary pressure \bar{p}^{n+1} is computed from the Poisson equation, derived from Eq. (5) by requiring incompressibility, with Neumann boundary conditions in which the diffusion term $\Delta \mathbf{V}^{n+1}$ is approximated using an Adams–Bashforth scheme. The Poisson problem to solve is therefore:

$$\begin{cases} \nabla^2 \bar{p}^{n+1} = \nabla \cdot [-2(\mathbf{V} \cdot \nabla \mathbf{V})^n + (\mathbf{V} \cdot \nabla \mathbf{V})^{n-1} + \mathbf{F}^{n+1}] & \text{in } D \\ \frac{\partial \bar{p}^{n+1}}{\partial n} = \mathbf{n} \cdot \left[\frac{-3\mathbf{W}^{n+1} + 4\mathbf{V}^n - \mathbf{V}^{n-1}}{2\delta t} - 2(\mathbf{V} \cdot \nabla \mathbf{V})^n + (\mathbf{V} \cdot \nabla \mathbf{V})^{n-1} \right. \\ \quad \left. + v(2\Delta \mathbf{V}^n - \Delta \mathbf{V}^{n-1}) + \mathbf{F}^{n+1} \right] & \text{on } \Gamma \end{cases} \quad (17)$$

However, this Poisson problem does not fulfil the compatibility condition, leading to an unstable algorithm. So, in order to satisfy the compatibility condition, the diffusion term has been treated as proposed by Karniadakis et al. [18]: the velocity Laplacian is then decomposed into a solenoidal part and an irrotational part. Since the velocity fields \mathbf{V}^n and \mathbf{V}^{n-1} are divergence free, the diffusion term writes:

$$2\Delta \mathbf{V}^n - \Delta \mathbf{V}^{n-1} = -2\nabla \times \nabla \times \mathbf{V}^n + \nabla \times \nabla \times \mathbf{V}^{n-1}$$

- *Prediction step*

As in the GPM, the predicted velocity field \mathbf{V}^* is computed implicitly from Eq. (5) in which the pressure gradient at the current time step t_{n+1} is now replaced by the gradient of the preliminary pressure:

$$\begin{cases} \frac{3\mathbf{V}^* - 4\mathbf{V}^n + \mathbf{V}^{n-1}}{2\delta t} + 2(\mathbf{V} \cdot \nabla \mathbf{V})^n - (\mathbf{V} \cdot \nabla \mathbf{V})^{n-1} = -\nabla \bar{p}^{n+1} + v\Delta \mathbf{V}^* + \mathbf{F}^{n+1} & \text{in } D \\ \mathbf{V}^* = \mathbf{W}^{n+1} & \text{on } \Gamma \end{cases} \quad (19)$$

- *Projection step*

The velocity field \mathbf{V}^* is then corrected by taking into account the pressure gradient at t_{n+1} so that the final velocity field satisfies the incompressibility constraint:

$$\begin{cases} \frac{3}{2\delta t}(\mathbf{V}^{n+1} - \mathbf{V}^*) = -\nabla(p^{n+1} - \bar{p}^{n+1}) & \text{in } \bar{D} \\ \mathbf{V}^{n+1} \cdot \mathbf{n} = \mathbf{W}^{n+1} \cdot \mathbf{n} & \text{on } \Gamma \\ \nabla \cdot \mathbf{V}^{n+1} = 0 & \text{in } D \end{cases} \quad (21)$$

$$\mathbf{V}^{n+1} \cdot \mathbf{n} = \mathbf{W}^{n+1} \cdot \mathbf{n} \quad \text{on } \Gamma \quad (22)$$

$$\nabla \cdot \mathbf{V}^{n+1} = 0 \quad \text{in } D \quad (23)$$

This step is performed by computing an intermediate variable $\varphi = 2\delta t(p^{n+1} - \bar{p}^{n+1})/3$ from a Poisson problem similar to Eqs. (13) and (14):

$$\begin{cases} \nabla^2 \varphi = \nabla \cdot \mathbf{V}^* & \text{in } D \\ \frac{\partial \varphi}{\partial n} = 0 & \text{on } \Gamma \end{cases} \quad (24)$$

$$\frac{\partial \varphi}{\partial n} = 0 \quad \text{on } \Gamma \quad (25)$$

The final velocity and pressure fields are then obtained from the formulas:

$$\begin{cases} \mathbf{V}^{n+1} = \mathbf{V}^* - \nabla \varphi \\ p^{n+1} = \bar{p}^{n+1} + \frac{3}{2\delta t} \varphi \end{cases} \quad \text{in } \bar{D} \quad (26)$$

- *Remarks*

The computation of the preliminary pressure and its introduction in the prediction step allow the normal pressure gradient at the boundary to vary with time. Indeed, at each time step, we have on the boundary:

$$\frac{\partial \varphi}{\partial n} = 0 \Rightarrow \frac{\partial p^{n+1}}{\partial n} = \frac{\partial \bar{p}^{n+1}}{\partial n} \quad \text{on } \Gamma$$

It must be noted that, as in the GPM, the velocity field \mathbf{V}^{n+1} computed by Eq. (26) fulfils the incompressibility constraint inside the computational domain D and the normal boundary conditions. On the other hand, it does not satisfy the tangential boundary conditions, which induces here again a slip velocity on the boundary. However, our results showed that this slip velocity is now $O(\delta t^3)$ (see Section 4.2). In the two-dimensional case, the slip velocity can be expressed as:

$$V_s = \boldsymbol{\tau} \cdot (\mathbf{V}^{n+1} - \mathbf{W}^{n+1}) = -\boldsymbol{\tau} \cdot \nabla \varphi = \frac{2\delta t}{3} \frac{\partial}{\partial \tau} (\bar{p}^{n+1} - p^{n+1}) \quad (27)$$

According to this formula, the slip velocity V_s is $O(\delta t^3)$ only if the difference $\bar{p}^{n+1} - p^{n+1}$ is $O(\delta t^2)$. Our tests on the exact unsteady solution (38)–(41) showed that this difference is actually $O(\delta t^2)$.

4. Numerical results for exact solutions

The variables are made dimensionless by taking $(b-a)/2$ and L as characteristic lengths in the radial and axial directions respectively, v/L as characteristic velocity and L^2/v as characteristic time. The geometric parameters are then the aspect ratio $G = (b-a)/(2L)$ and the curvature parameter $R_c = (b+a)/(b-a)$, and the physical parameter is the Reynolds number $Re = 2\Omega(b-a)^2/v$. In a reference frame rotating at angular velocity Ω , the dimensionless Navier–Stokes equations write:

$$\begin{aligned} \frac{\partial u}{\partial t} + \frac{u}{G} \frac{\partial u}{\partial Y} + \frac{v}{G(Y+R_c)} \frac{\partial u}{\partial \theta} + w \frac{\partial u}{\partial Z} - \frac{v^2}{G(Y+R_c)} - \frac{Re}{4G^2} v \\ = -\frac{1}{G} \frac{\partial p}{\partial Y} + \nabla^2 u - \frac{u}{G^2(Y+R_c)^2} - \frac{2}{G^2(Y+R_c)^2} \frac{\partial v}{\partial \theta} + F_u \end{aligned} \quad (28)$$

$$\begin{aligned} \frac{\partial v}{\partial t} + \frac{u}{G} \frac{\partial v}{\partial Y} + \frac{v}{G(Y+R_c)} \frac{\partial v}{\partial \theta} + w \frac{\partial v}{\partial Z} + \frac{uv}{G(Y+R_c)} + \frac{Re}{4G^2} u \\ = -\frac{1}{G(Y+R_c)} \frac{\partial p}{\partial \theta} + \nabla^2 v - \frac{v}{G^2(Y+R_c)^2} + \frac{2}{G^2(Y+R_c)^2} \frac{\partial u}{\partial \theta} + F_v \end{aligned} \quad (29)$$

$$\frac{\partial w}{\partial t} + \frac{u}{G} \frac{\partial w}{\partial Y} + \frac{v}{G(Y+R_c)} \frac{\partial w}{\partial \theta} + w \frac{\partial w}{\partial Z} = -\frac{\partial p}{\partial Z} + \nabla^2 w + F_w \quad (30)$$

$$\frac{1}{G} \frac{\partial u}{\partial Y} + \frac{u}{G(Y+R_c)} + \frac{1}{G(Y+R_c)} \frac{\partial v}{\partial \theta} + \frac{\partial w}{\partial Z} = 0 \quad (31)$$

where $\mathbf{F} = (F_u, F_v, F_w)$ is a source term computed from the chosen exact solution (\mathbf{V}_e, p_e) and:

$$\nabla^2 = \frac{1}{G^2} \left(\frac{\partial^2}{\partial Y^2} + \frac{1}{Y+R_c} \frac{\partial}{\partial Y} + \frac{1}{(Y+R_c)^2} \frac{\partial^2}{\partial \theta^2} \right) + \frac{\partial^2}{\partial Z^2}$$

The tests reported in the following sections were performed with the parameters values $G = 1$, $R_c = 2$ and $Re = 500$.

4.1. Exact steady solution

First, the space accuracy of the two projection methods was checked on the exact steady solution defined in $\bar{D} = [-1, +1] \times [0, 2\pi[\times [-1, +1]$ by:

$$u_e(Y, \theta, Z) = \frac{1}{2\pi} (\sin(\pi Y))^2 \sin(2\pi Z) \cos(\theta) \quad (32)$$

$$v_e(Y, \theta, Z) = -\frac{1}{2\pi} (\sin(\pi Y))^2 \sin(2\pi Z) \sin(\theta) \quad (33)$$

$$w_e(Y, \theta, Z) = -\frac{1}{2\pi G} \sin(2\pi Y) (\sin(\pi Z))^2 \cos(\theta) \quad (34)$$

$$p_e(Y, \theta, Z) = [\cos(\pi Y) + \cos(\pi Z)] \cos(\theta) \quad (35)$$

The velocity field \mathbf{V}_e is actually divergence free and satisfies homogeneous Dirichlet boundary conditions. The space accuracy of the algorithms was evaluated by computing the L_2 discrete errors at the inner collocation points, $\text{Er}(\Phi)$, and at the boundary collocation points, $\text{Er}_B(\Phi)$, for $\Phi = u, v, w, p$. The slip velocity is evaluated by computing the L_2 discrete norm of one component of the tangential velocity at boundaries $Y = \pm 1$ and $Z = \pm 1$ i.e.:

$$\|V_\tau\|_B = \frac{1}{2K(N+M-2)} \sum_{q=-K/2}^{K/2-1} \left[\sum_{i=1}^{N-1} u_{KNM}(Y_i, \theta_q, \pm 1)^2 + \sum_{j=1}^{M-1} w_{KNM}(\pm 1, \theta_q, Z_j)^2 \right]^{1/2}.$$

The main weakness of the GPM lies in the fact that the normal pressure gradient at the boundary is held at its initial value. In order to study the influence of this initial value on the space accuracy of the algorithm, two initial conditions for the velocity were considered:

$$\text{IC1: } \mathbf{V}_0 = (0, 0, 0) \quad (36)$$

$$\text{IC2: } \mathbf{V}_0 = \mathbf{V}_e + \frac{1}{200\pi^2} \mathbf{V}_e \quad (37)$$

For the first initial condition, the maximum of the difference between the initial pressure gradient at the boundary, $\partial p_0/\partial n$, and the exact one, $\partial p_e/\partial n$, is equal to π , whereas, in the case of IC2, this maximum is 1.6×10^{-3} . For the modified projection method (MPM), only the initial condition IC1 was used.

The steady solution is assumed to be obtained when the residual $\text{Res}(\Phi) = \max_{(i,j,q)} |\Phi_{KNM}^n(Y_i, \theta_q, Z_j) - \Phi_{KNM}^{n-1}(Y_i, \theta_q, Z_j)|/\delta t$ reaches 10^{-12} for the velocity components and 10^{-9} for the pressure. For all the resolutions tested, the time step used is $\delta t = 5 \times 10^{-3}$.

The values of the error at the inner collocation points are reported for the radial velocity component u and for the pressure in Fig. 1a. For the solution computed with the MPM, these errors exhibit an exponential decay, which is characteristic of spectral approximations, and they reach the machine accuracy for $N = M = K = 32$. On the other hand, a very slow decay is observed for the GPM and the machine accuracy is never obtained even for the largest resolution. However, when the initial condition IC2 is used, $\text{Er}(u)$ and $\text{Er}(p)$ seem to exhibit an exponential

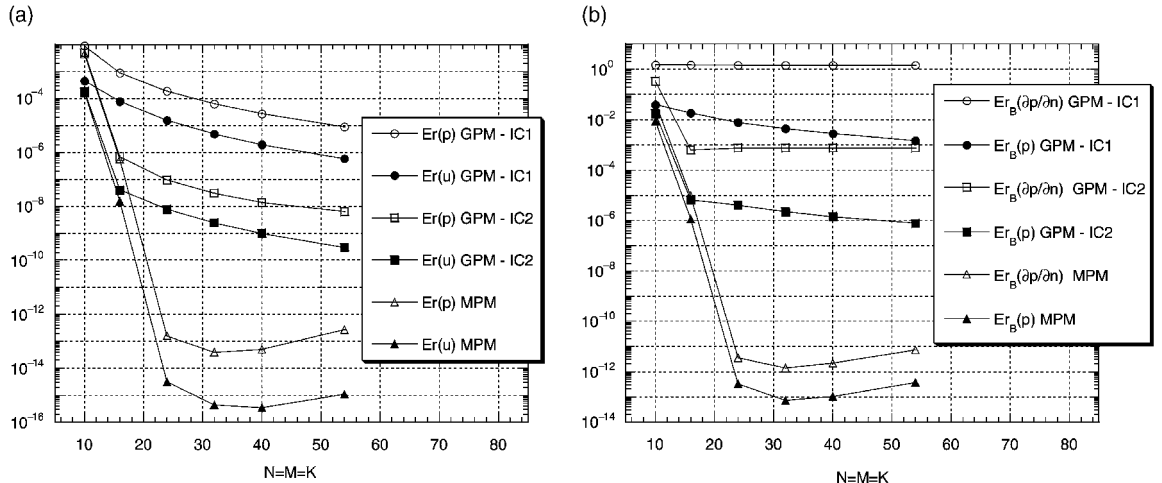


Fig. 1. Space accuracy of the GPM and of the MPM for a 3D stationary exact solution. (a) Evolution of the error $\text{Er}(\Phi)$ for the radial velocity component u and for the pressure p , versus the polynomial degrees $N = M = K$. (b) Evolution of the error $\text{Er}_B(\Phi)$ on the boundary for the pressure and for the normal pressure gradient, versus the polynomial degrees $N = M = K$.

decay for $N \times M \times K \leq 16 \times 16 \times 16$ before decreasing slowly (with the same slope as the one observed in the case of IC1) for the larger resolutions. The same behaviour was obtained for the errors $\text{Er}(v)$ and $\text{Er}(w)$.

Fig. 1a shows also that the values of the errors depend strongly on the difference between the initial and the exact pressure gradients on the boundary. For $N = M = K = 54$, $\text{Er}(u)$ and $\text{Er}(p)$ are about 6×10^{-7} and 8×10^{-6} respectively when IC1 is used whereas they are almost three orders of magnitude smaller with the initial condition IC2.

A similar difference of behaviours between the GPM and the MPM is noted on the error at boundaries for the pressure (Fig. 1b). The fundamental difference between the GPM and the MPM can be clearly seen on the error of the normal pressure gradient on the boundary (Fig. 1b). The MPM allows the normal pressure gradient to vary with time in order to recover the one of the exact solution whatever the initial condition is. Indeed, $\text{Er}_B(\partial p / \partial n)$ exhibits an exponential decay and it reaches the machine accuracy for $N = M = K = 32$. On the other hand, for the solution computed with the GPM, $\text{Er}_B(\partial p / \partial n)$ remains constant for all the resolutions tested when using the initial condition IC1. When IC2 is used (for which $\max |\partial p_0 / \partial n - \partial p_e / \partial n|$ is about a thousand times smaller than for IC1), $\text{Er}_B(\partial p / \partial n)$ decreases for $N \times M \times K \leq 16 \times 16 \times 16$ before remaining constant for larger resolutions. In fact, for $N \times M \times K \leq 16 \times 16 \times 16$, the error due to the space approximation is larger than the initial error $\text{Er}_B(\partial p_0 / \partial n)$, which explains the decrease of $\text{Er}_B(\partial p / \partial n)$ and also the fast decay of $\text{Er}(u)$, $\text{Er}(p)$ and $\text{Er}_B(p)$.

We have pointed out above that, when the polynomial degree is sufficiently large to represent the solution (i.e. for $N = M = K \geq 16$), the errors $\text{Er}(u)$ and $\text{Er}(p)$ for the GPM decrease slowly, when increasing the resolution, with the same slope for the two initial conditions tested. In order to bring to the fore more precisely the effect of the initial pressure gradient at the boundary on the computed solution, tests were carried out with different initial conditions for the velocity such that $1.6 \times 10^{-3} \leq \max |\partial p_0 / \partial n - \partial p_e / \partial n| \leq 200$. The polynomial degrees were fixed to $N = M = K = 40$. The results, reported in Fig. 2, show that the errors $\text{Er}(u)$ and $\text{Er}(p)$ increase linearly with $\max |\partial p_0 / \partial n - \partial p_e / \partial n|$.

From their definition, the two projection methods satisfy exactly the incompressibility constraint inside the computational domain. We have checked that the velocity fields computed with the GPM and the MPM are actually divergence free with a discrete norm $\|\nabla \mathbf{V}_{KNM}\|_1$ ranging from 10^{-9} to 10^{-14} for the GPM and from 10^{-9} to 10^{-16} for the MPM, when increasing the resolution. On the other hand, the incompressibility constraint is not prescribed on the boundary. However, Fig. 3a shows that the discrete norm of the velocity divergence for the MPM reaches the machine accuracy for $N = M = K = 32$. On the other hand, for the GPM, $\|\nabla \mathbf{V}_{KNM}\|_B$ exhibits a very slow decay when increasing the resolution and it is only about 10^{-3} (7×10^{-7} respectively) for $N = M = K = 54$ when using IC1 (IC2 respectively).

Finally, the discrete norm of the slip velocity is reported in Fig. 3b. For the GPM, $\|\mathbf{V}_\tau\|_B$ varies from 10^{-17} for the lowest resolution to 7×10^{-12} for the highest one. For the MPM, $\|\mathbf{V}_\tau\|_B$ exhibits an exponential decay and it reaches the machine accuracy for $N = M = K = 32$. So, for resolutions $N \times M \times K \leq 24 \times 24 \times 24$, the slip velocity induced by the MPM is much larger than the one obtained with the GPM. This is due to the fact that, when the steady solution is reached, the difference $p^{n+1} - \bar{p}^{n+1}$ does not converge to zero (on the contrary of $p^{n+1} - p^n$) for small resolutions. Indeed, we observed that $\|\mathbf{V}_\tau\|_B$ follows the same decay as $\|p^{n+1} - \bar{p}^{n+1}\|_B$ when increasing the polynomial degrees.

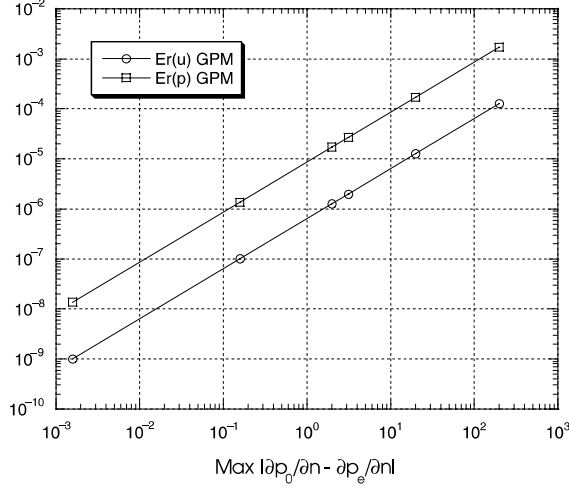


Fig. 2. Space accuracy of the GPM for a 3D stationary exact solution. Variation of the errors $Er(u)$ and $Er(p)$ with the maximum of the difference between the initial and the exact pressure gradients on the boundary for the polynomial degrees $N = M = K = 40$.

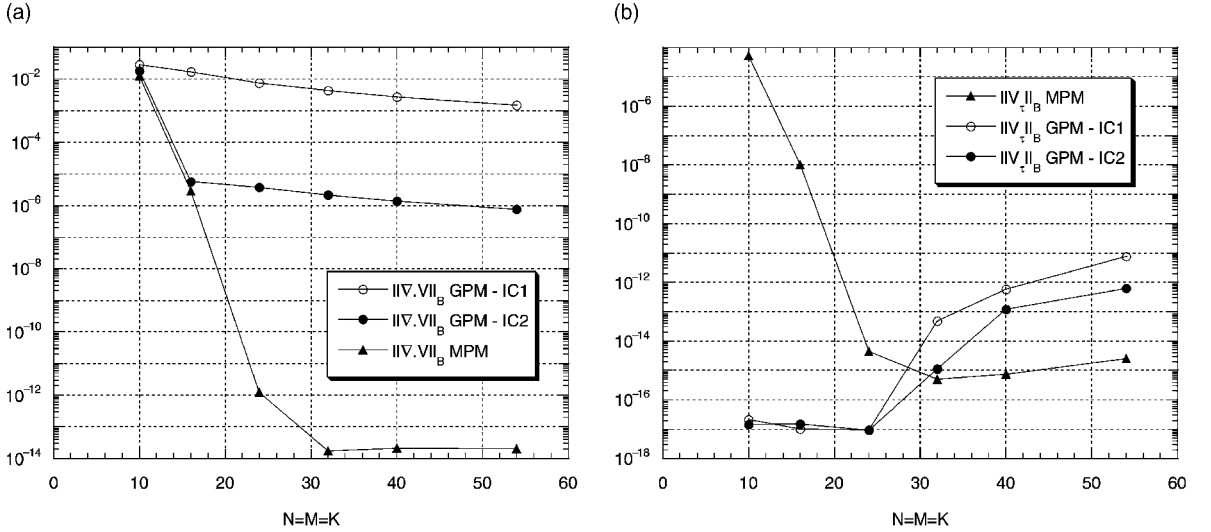


Fig. 3. Space accuracy of the GPM and of the MPM for a 3D stationary exact solution. (a) Evolution of the discrete norm of the velocity divergence on the boundary versus the polynomial degrees $N = M = K$. (b) Evolution of the discrete norm of the slip velocity versus the polynomial degrees $N = M = K$.

4.2. Exact time-dependent solution

The time accuracy of the two projection methods was checked on the exact time-dependent solution defined in $\bar{D} = [-1, +1] \times [0, 2\pi \times [-1, +1]]$ by:

$$u_e^i(Y, \theta, Z, t) = u_e(Y, \theta, Z)(\cos(4\pi t)^2 + 1) \quad (38)$$

$$v_e^i(Y, \theta, Z, t) = v_e(Y, \theta, Z)(\cos(4\pi t)^2 + 1) \quad (39)$$

$$w_e^i(Y, \theta, Z, t) = w_e(Y, \theta, Z)(\cos(4\pi t)^2 + 1) \quad (40)$$

$$p_e^i(Y, \theta, Z, t) = p_e(Y, \theta, Z)(\cos(4\pi t)^2 + 1) + A(Y + Z) \cos(\theta) \cos(4\pi t) \quad (41)$$

This solution is time periodic with a period $T = 0.25$. It is used to define the initial condition for the velocity $\mathbf{V}_0 = \mathbf{V}_e$ ($t = 0$). On the boundary, the normal pressure gradient is given by:

$$\frac{\partial p_e^i}{\partial n} = A \cos(\theta) \cos(4\pi t) \quad \text{on } \Gamma$$

So, when $A \neq 0$, the normal pressure gradient of the exact solution varies with time on the boundary. The two projection methods are compared for $A = 0$ and 10. When $A = 10$, the maximum during time between the initial and the exact normal pressure gradients on the boundary is equal to 20. A comparison with the initial Chorin–Temam method is also performed in the case $A = 10$.

The polynomial degrees were fixed to 40 in each space direction in order to ensure a sufficiently high space accuracy. The time step was then decreased from $\delta t = 5 \times 10^{-3}$ to $\delta t = 5 \times 10^{-5}$. When the periodic state is reached, the time accuracy is evaluated by computing the temporal maximum of the L_2 discrete errors at the inner collocation points, $\text{Er}^i(\Phi)$, and at the boundary collocation points, $\text{Er}_B^i(\Phi)$. In the same way, the slip velocity is evaluated by computing the maximum value during time of $\|\mathbf{V}_\tau(t)\|_B$.

The results are presented in Figs. 4–6. When there is no pressure gradient variation in time on the boundary (i.e. $A = 0$), the two projection methods exhibit the same temporal behaviour in $\mathcal{O}(\delta t^2)$ for the radial velocity component and for the pressure inside the computational domain (Fig. 4) and also for the pressure on the boundary (Fig. 5a). The same temporal behaviour was observed for the azimuthal and axial velocity components.

The basic difference between the GPM and the MPM can be clearly seen on the variation of the errors when the exact solution presents a time-dependent pressure gradient on the boundary ($A = 10$). The second-order accuracy is still obtained for both the radial velocity and the pressure computed with the MPM (Figs. 4 and 5a). On the other hand, for the GPM, the errors $\text{Er}^i(u)$ and $\text{Er}^i(p)$ exhibit a temporal behaviour in $\mathcal{O}(\delta t^2)$ for $\delta t \geq 10^{-3}$, and then they remain constant for smaller time steps (Fig. 4). The same saturation is observed for the error on the pressure on the boundary (Fig. 5a). This saturation of the errors was observed elsewhere for a 2D analytic solution [17]. It is due to the error in space induced by the incorrect treatment of the pressure gradient on the boundary. Indeed, it can be noted that the saturation value of $\text{Er}^i(u)$ is almost the same as the error $\text{Er}(u)$ obtained for the steady exact solution when $\max |\partial p_0 / \partial n - \partial p_e / \partial n| = 20$ (Fig. 2). The saturation value of $\text{Er}^i(p)$ is larger than the error $\text{Er}(p)$ reported in Fig. 2, but the time-dependent analytic pressure (41) has a spatial part different from the one of the steady solution (35) (because of the term $A(Y + Z) \cos(\theta) \cos(4\pi t)$). When increasing the resolution up to $N \times M \times K = 54 \times 54 \times 54$, the space error is smaller and the temporal behaviour in $\mathcal{O}(\delta t^2)$ of the errors $\text{Er}^i(u)$ and $\text{Er}^i(p)$ is obtained until $\delta t = 5 \times 10^{-4}$ (Fig. 4). This confirms the fact that the

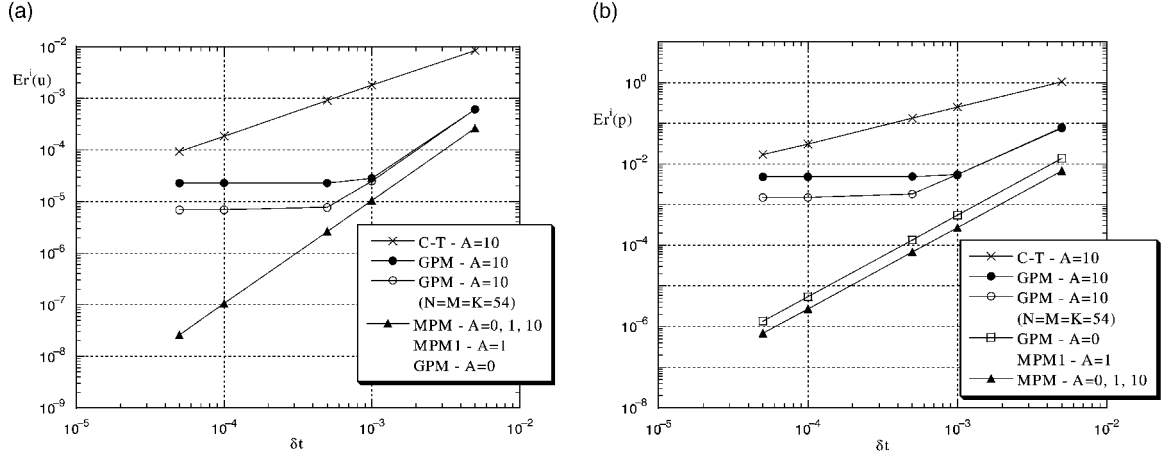


Fig. 4. Time accuracy of the Chorin–Temam method (C–T), of the GPM, of the MPM and of the MPM1. Evolution of the error $Er^i(\Phi)$ for a 3D time-dependent exact solution (a) for the radial velocity component u and (b) for the pressure, versus the time step δt .

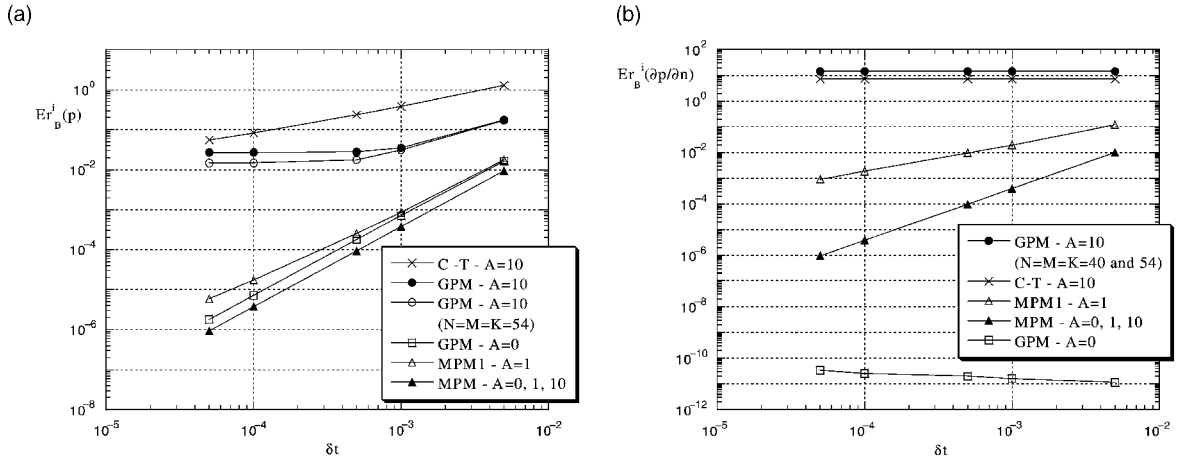


Fig. 5. Time accuracy of the Chorin–Temam method (C–T), of the GPM, of the MPM and of the MPM1. Evolution of the error $Er_B^i(\Phi)$ on the boundary for a 3D time-dependent exact solution (a) for the pressure and (b) for the normal pressure gradient, versus the time step δt .

saturation of the errors is due to the error in space. It must be noted that all the behaviours mentioned above for the radial velocity are also observed for the azimuthal and the axial velocity components. However, in spite of the bad behaviour of the GPM, the errors obtained with this method are smaller than the ones given by the initial Chorin–Temam algorithm which ensures only a first-order accuracy (Fig. 4).

Fig. 5b shows clearly the difference of behaviour resulting from the treatment of the pressure gradient on the boundary between the GPM and the MPM. For the GPM (as for the Chorin–Temam method), $Er_B^i(\partial p/\partial n)$ remains constant for all the time steps whereas a temporal behaviour in $O(\delta t^2)$ is obtained with the MPM.

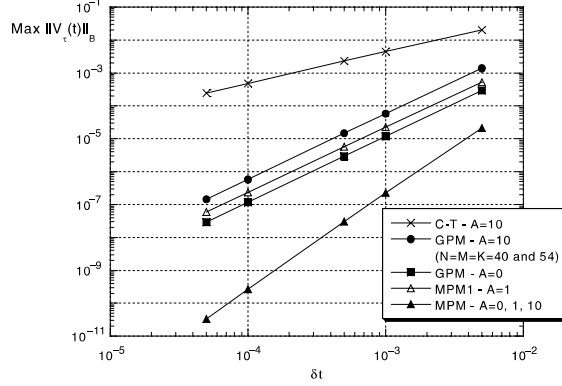


Fig. 6. Time accuracy of the Chorin–Temam method (C–T), of the GPM, of the MPM and of the MPM1. Evolution of the temporal maximum of the discrete norm of the slip velocity versus the time step δt , for a 3D time-dependent exact solution.

4.2.1. Slip velocity

Another improvement brought by the MPM concerns the slip velocity. For all the exact solutions tested (with $A = 0$ or 10), the temporal maximum of $\|\mathbf{V}_\tau(t)\|_B$ is $O(\delta t^3)$ with the MPM whereas it is only $O(\delta t^2)$ with the GPM, in accordance with Eq. (16) (Fig. 6). This is explained by the fact that the temporal maximum of $\|p^{n+1} - \bar{p}^{n+1}\|_B$ is $O(\delta t^2)$ for the MPM, which induces a behaviour in $O(\delta t^3)$ for the slip velocity, according to Eq. (27). Fig. 6 shows also that the Chorin–Temam method exhibits a $O(\delta t)$ slip velocity.

The slip velocity is generated by the projection step in which only the boundary condition for the normal component of the velocity is prescribed. Then, it is taken into account in the computation of the convective terms $\nabla \cdot \nabla \mathbf{V}$ since it appears in the reconstruction of the final velocity at the previous time steps through Eqs. (15) and (26). However, it is possible to prescribe the actual boundary conditions for \mathbf{V}^{n+1} by replacing these equations by:

$$\begin{cases} \mathbf{V}^{n+1} \cdot \mathbf{n} = \mathbf{V}^* \cdot \mathbf{n} - \nabla \varphi \cdot \mathbf{n} & \text{in } \bar{D} \\ \mathbf{V}^{n+1} \cdot \boldsymbol{\tau} = \mathbf{V}^* \cdot \boldsymbol{\tau} - \nabla \varphi \cdot \boldsymbol{\tau} & \text{in } D \\ \mathbf{V}^{n+1} \cdot \boldsymbol{\tau} = \mathbf{W}^{n+1} \cdot \boldsymbol{\tau} & \text{on } \Gamma \end{cases} \quad (42)$$

A similar modification was tested by Strikwerda and Lee [32] for the projection method proposed by Kim and Moin [19]. They observed that the same order of accuracy is obtained with and without this modification.

We have used Eq. (42) with the GPM as well as with the MPM. In the case of the GPM, using formulae (42) or (15) gives exactly the same results in terms of stability and accuracy. On the other hand, the MPM becomes unstable when the final velocity is computed by Eq. (42). In fact, for the MPM, the slip velocity appears not only in the source term of the Helmholtz equation for \mathbf{V}^* (through the convective term) but also in the boundary condition of the preliminary pressure through the terms $-2(\nabla \cdot \nabla \mathbf{V})^n + (\nabla \cdot \nabla \mathbf{V})^{n-1}$ and $-2\nabla \times \nabla \times \mathbf{V}^n + \nabla \times \nabla \times \mathbf{V}^{n-1}$. When the diffusion term was written in the Laplacian form in the boundary condition of \bar{p}^{n+1} , convergence

was obtained for the MPM only for $\delta t \leq 5 \times 10^{-4}$ and the temporal maximum of $\|\nabla \mathbf{V}^{n+1}\|_{\mathbb{B}}$ was about one hundred times larger than the one obtained when using Eq. (26). So, using formulas (42) for the MPM leads in all the cases to a loss of stability and/or to a loss of accuracy.

4.2.2. Splitting error

The splitting error introduced by the MPM is $2\delta t v \nabla^2(\nabla(p^{n+1} - \bar{p}^{n+1}))/3$ which is $O(\delta t^3)$ since $p^{n+1} - \bar{p}^{n+1}$ is $O(\delta t^2)$. So it is smaller by one order of magnitude than that induced by the GPM which is $O(\delta t^2)$. Nevertheless, we tried to construct an algorithm free of this splitting error. To this end, we followed the same approach as Kim and Moin's one for their algorithm [19]. Namely, Eq. (21) in the projection step is replaced by:

$$\frac{3}{2\delta t}(\mathbf{V}^{n+1} - \mathbf{V}^*) = -\gamma \nabla \Phi \quad \text{in } D$$

with $\gamma \geq 1$. The projection step is then solved through a Poisson problem for this new variable Φ and the final pressure is built so that the splitting error is equal to zero:

$$p^{n+1} = \bar{p}^{n+1} + \gamma \Phi - \frac{2\delta t}{3} v \gamma \nabla^2 \Phi \quad \text{in } \bar{D}$$

Three values of the parameter γ were considered ($\gamma = 1, 1.5, 2$) but no real influence was observed. The tests showed that this new algorithm is neither more stable nor more accurate than the MPM, since the errors obtained with the two methods are almost the same.

4.2.3. Accuracy of the preliminary step

In order to study the effect of the temporal scheme used for the diffusion term in the boundary condition (18) on the accuracy of the solution, tests were performed with $\Delta \mathbf{V}^n$ used for the approximation of $\Delta \mathbf{V}^{n+1}$ instead of the Adams–Bashforth scheme. The resulting algorithm is called the first order MPM (MPM1). As for the MPM, the diffusion term in the boundary condition of the preliminary pressure is written in the form $\nabla \times \nabla \times \mathbf{V}^n$ in order to ensure stability. The comparison with the MPM was performed on the exact solution (38)–(41) with $A = 1$. The results are reported on Figs. 4–6.

Fig. 4 reveals that the two methods exhibit the same behaviour in $O(\delta t^2)$ for the radial velocity and for the pressure inside the computational domain, with an error for the pressure slightly larger with the MPM1. On the other hand, the second order accuracy on the boundary is lost for the MPM1. The errors $\text{Er}_{\mathbb{B}}^i(p)$ and $\text{Er}_{\mathbb{B}}^i(\partial p / \partial n)$ are only $O(\delta t^{1.8})$ and $O(\delta t)$ respectively. Moreover the error $\text{Er}_{\mathbb{B}}^i(\partial p / \partial n)$ is much larger than the one generated by the MPM. In the same way, the slip velocity induced by the MPM1 recovers the behaviour in $O(\delta t^2)$ of the GPM. This is due to the fact that the difference $p^{n+1} - \bar{p}^{n+1}$ is now $O(\delta t)$ whereas it was $O(\delta t^2)$ with the MPM. Consequently, it is necessary to use a second order scheme for the approximation of the diffusion term in the boundary condition of the preliminary pressure if one wants to obtain a real improvement in terms of accuracy on the boundary with regards to the Goda's method.

5. Application to complex rotating flows

The MPM has been applied to the study of three-dimensional instability phenomena of boundary layers involved in rotating systems. Two configurations were considered: a rotating cavity with a superposed radial outflow (the two disks spaced by $2L$ rotating at the same angular speed Ω) and an enclosed rotor–stator annular and interdisk cavity (the lower disk being stationary and the upper one rotating with the angular speed Ω). A detailed study of the physical results can be found in Refs. [27,28]. In the framework of the present paper, we only report the major features in order to show the efficiency of the MPM.

The scales for the dimensionless variables are L for length, Ω^{-1} for time and Ωb for velocity. The two geometric parameters are the aspect ratio $G = (b - a)/(2L)$ and the curvature parameter $R_c = (b + a)/(b - a)$. The relevant physical parameters are the Reynolds number defined here by $Re = \Omega(2L)^2/\nu$ and, when the flow is submitted to a radial forced flow, the dimensionless parameter $C_w = Q/vb$, with Q the mass flow rate. In all the cases, the boundary conditions correspond to no-slip conditions for u and w at the rigid walls. For the open cavity, an Ekman boundary layer flow [15] is considered as inflow and outflow. For the rotor–stator cavity, the boundary conditions of the azimuthal velocity component are $v = 0$ on the stator and $v = (R_c + r)/(R_c + 1)$ on the rotating disk. In order to suppress the singularity of the azimuthal velocity condition at the junction between the stationary cylindrical envelope and the rotor, a linear azimuthal velocity profile is imposed on the inner and outer cylinders, called respectively the shaft and the shroud.

A characteristic of the flows developing in such rotating systems is the co-existence of adjacent and coupled flow regions which are very different in terms of flow properties and of the length scales as it is the case for the Ekman (on a rotating disk) or Bödewadt (on a stationary disk) boundary layers and the geostrophic core region. Two classes of generic instabilities develop above rotating and/or stationary disks that are referred in the literature according to the standard terminology type I and type II [13]. The type I instability, also called ‘crossflow’, is associated with the presence of inflection points in the normal velocity profiles to the disk plane (i.e. the radial velocity profiles in our case). On the other hand, Lilly [20] showed, using a linear stability analysis, that the type II instability, appearing at lower values of the critical Reynolds number and with a larger wavelength, is related to the combined effects of the Coriolis and viscosity forces.

In our simulations, the spatial structure of instabilities are displayed by the velocity fluctuations computed from the numerical solutions at given instants with respect to the average flow. The dynamic behaviour of the variables is analysed at several significant locations in each boundary layer and in the geostrophic core. The radial wavelength is defined by $\lambda_r = (b - a)/n_r$, where n_r is the number of vortices pairs along the radius. On the other hand, for the spiral patterns, the general wavelength is defined by $\lambda = 2\pi r |\sin(\varepsilon)|/n$ where n is the number of spiral arms over 2π at the radius r and ε is the angle of the wave front with the geostrophic velocity (it is defined positive when it is rolled up towards the axis of the disk in the rotation direction). The wavelength is sized in terms of the length scale of the Ekman layer $\delta = (\nu/\Omega)^{1/2}$, as it is usual in the literature.

The results were obtained using resolutions up to $N \times M \times K = 64 \times 64 \times 128$, depending on the values of the mass flow rate C_w (for the open rotating cavity) or the Reynolds number Re (for the rotor–stator cavity). The time steps used are $\delta t = 4 \times 10^{-3}$ and 2×10^{-3} , depending on the

resolution. For time-dependent solutions, the computing time is sized at the level of the largest characteristic time in rotating flows, i.e. the viscous time $t_v = L^2/\nu$ [13].

5.1. Rotating cavity with radial outflow

The base flow solution is stationary and axisymmetric and corresponds to the Ekman layer flow. For this type of flow, the Coriolis force dominates with respect to inertial and centrifugal forces near the walls. The flow organizes itself symmetrically and parallel Ekman boundary layers form on the two rotating disks with the same mass flow rate [27]. In the numerical solutions, the meridian flow in (r, z) mainly concentrates near these two Ekman layers while outside, in the geostrophic core, the Coriolis force balances the pressure force and the flow is mainly governed by an azimuthal flow. All the results presented in this section were obtained with the geometric parameters $G = 3.37$ and $R_c = 5$ and the Reynolds number $Re = 1750$.

Multiple periodic solutions with different numbers of spiral arms were obtained for a same value of C_w . The spiral patterns with eight arms are presented in Fig. 7. The wave front angle ε with the geostrophic velocity is negative (about -10°). Due to the computational cost, the transition to three-dimensional patterns was not carried out actually over very large time stages but it was accelerated by introducing ‘artificial’ initial disturbances. The general form of these disturbances is $\alpha \sin(p\theta)$ where p is an arbitrary number, corresponding to an azimuthal wavelength, and α is the amplitude coefficient ($\alpha = 0.05$ generally). The disturbance is superposed to the axisymmetric solution locally near the entry section. We noted that the number n of spiral arms follows the periodicity of the disturbance, $n \geq p$ for $p \geq (b - a)/\lambda_r$ (≈ 6) [27]. The solutions are stable to further disturbances with $p \neq n$. On the other hand, we noted that the angular frequency σ increases with the number of arms, $\sigma \propto n$. These 3D spiral patterns have been already observed in experiments on Ekman layer flows and the characteristic parameters are in good agreement with those obtained by Caldwell and Van Atta [3] and Faller and Kaylor [5]. Moreover, the present results are quite similar to those given by the stability analysis in the case of an infinite disk [6]. Thus, the spiral structure of the computed rotor layer flow exhibits the same characteristics as the type II instability of the Ekman boundary layer.

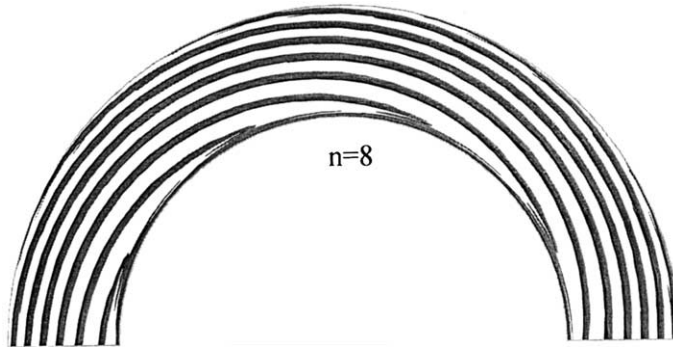


Fig. 7. Rotating cavity with radial outflow. Three-dimensional displays of instantaneous iso-surfaces of the axial velocity component, for $0 < z \leq 1$, projected in a plane (r, θ) , $0 \leq \theta \leq \pi$, for $C_w = 530$ and $Re = 1750$. Spiral patterns with eight arms.

5.2. Rotor–stator cavity

In the case of a rotor–stator cavity, the base flow is a Batchelor flow, composed by two separate boundary layers above each disk, with an outflow on the rotating disk (i.e. the radial velocity component is positive) and an inflow on the stationary disk (i.e. the radial velocity component is negative). These boundary layers are separated by a geostrophic core in solid body rotation (the authors refer to Ref. [28] for more details). By analogy with the single disk case, the layer over the rotating disk is called Ekman layer and the other one, on the stationary disk, is called Bödewadt layer. The results presented below were obtained in cavities with an aspect ratio $G = 5$ and a curvature parameters $R_c = 4$.

- *Axisymmetric annular instabilities*

Two kinds of axisymmetric instabilities have been simulated succeeding to the stationary base flow. The first one, obtained for $Re = 330$, is a stationary instability on the Bödewadt layer, characterized by three pairs of circular rolls (with $6 \leq \lambda_r/\delta \leq 11$). This instability has never been obtained numerically before. This stationary solution exhibits characteristics closely similar to the instability phenomenon observed in the experiments of Sirivat [31] which were carried out for a cylindrical interdisk cavity (i.e. without the inner cylinder) of $G = 10.52$. Sirivat observed, for $Re = 88.6$, stationary circular rolls of wavelength $9.4 \leq \lambda_r/\delta \leq 14$, related to the type II instability of the Bödewadt layer.

When further increasing the rotation rate, the instability becomes time-dependent. For $Re = 400$, the solution is oscillatory with a fundamental frequency $\sigma = 4.7$. The axisymmetric vortices are visible along the two layers on both disks and travel following the flow (Fig. 8). Inside the Ekman layer, three pairs of large size circular rolls (with $19.5 \leq \lambda_r/\delta \leq 30$) arise, whereas, in the Bödewadt layer, the solution exhibits about five pairs of counter-rotating rolls (with $11 \leq \lambda_r/\delta \leq 17.6$). The vortices move with a radial phase velocity $V_\phi = \lambda_r \sigma / (2\pi)$, which slightly decreases with the radial location such as $0.08 \leq V_\phi / \Omega r \leq 0.12$. Recent experiments of Gauthier et al. [8] and Schouveiler et al. [26] report about the same kind of oscillatory axisymmetric patterns in a cylindrical cavity, but far from the axis. Typical angular frequency and wavelength are then $\sigma = 4$ and $\lambda_r/\delta = 25.4$ for $Re = 128$ in a cavity of large aspect ratio ($G = 10.45$).

- *Three-dimensional spiral instabilities*

The same disturbance as the one used for the study of the open cavity was superposed to the axisymmetric solution, locally near the outer cylinder (more precisely for $G(R_c + 0.7) \leq r \leq G(R_c + 1)$). We noted that the three disturbances, of respective azimuthal wavelength

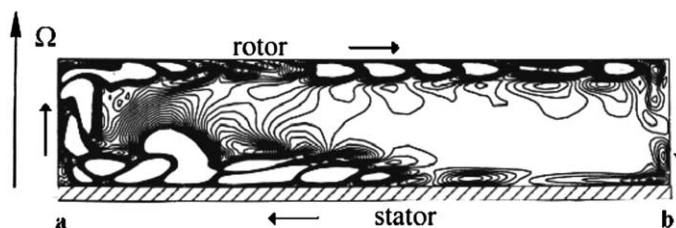


Fig. 8. Rotor–stator cavity. Axisymmetric time-dependent instability for $Re = 400$. Iso-lines of the fluctuation of the axial velocity.

$p = 2\pi/3$, $2\pi/8$ and $2\pi/12$, give rise to the same three-dimensional solution. The rolls, which progressed as rings in the case of the axisymmetric solution, form now spiral arms and expand inside the cavity.

For $Re = 400$, we observed the co-existence of spiral and annular structures inside the Bödewadt layer and dislocations near the rotating disk (Fig. 9). The time history reveals two major frequencies of different magnitude in the different regions of the cavity. We noted that the smallest frequency $\sigma_2 = 8$ is dominant magnitude in the stationary disk layer whereas the larger one $\sigma_1 = 16.2$ is conversely dominant in the rotating disk layer and at the rotor–shroud corner. On the other hand, both frequencies are of same magnitude at the rotor–shaft and stator–shroud corners. Inside the Ekman layer, we observed seven pairs of rolls in the radial direction and 18 spiral arms in the azimuthal direction with an angle ε which steeply decreases between a and b from -20° to -7.5° . The associate wavelength increases in the range $11.4 \leq \lambda/\delta \leq 17.9$. The vortices travel outward with a phase velocity V_ϕ such as $0.12 \leq V_\phi/\Omega r \leq 0.30$. The spiral structures have characteristic parameters (λ, ε) relevant to a type II instability. Inside the Bödewadt layer, we observed four pairs of spiral and annular rolls with an average radial wavelength $\lambda_r/\delta = 19.2$ and two pairs close to the shroud with a larger wavelength $\lambda_r/\delta = 26$. The latter develops in rings whereas the first one develops into 18 spiral arms which form an angle ε such as $15.6^\circ \leq \varepsilon \leq 23^\circ$ close to the shaft (more precisely for $15 \leq r \leq 18$). The persisting axisymmetric structures interact with the spiral arms at $r = 18$ and travel inward with a radial phase velocity V_ϕ such as $0.19 \leq V_\phi/\Omega r \leq 0.27$. The co-existence of spiral and annular structures was first described by Savas [25] who reported patterns involving simultaneously spiral waves with 23 arms of positive angle and circular waves during a transient spin down. Savas identified these spirals to the type I instability of the Bödewadt layer. The axisymmetric structures were observed close to the external wall as it is the case in our numerical solution.

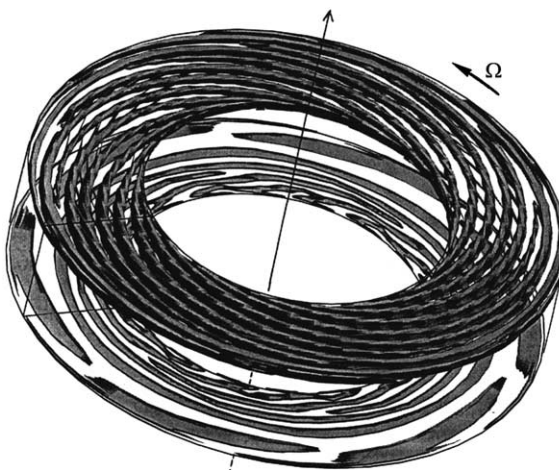


Fig. 9. Rotor–stator cavity. Complex spiral and annular patterns of the instability for $Re = 400$. Three-dimensional displays of iso-surfaces of the axial velocity component fluctuation in both Ekman and Bödewadt layers.

6. Conclusion

We have presented an efficient projection method to solve the three-dimensional incompressible Navier–Stokes equations using a Chebyshev–collocation–Fourier approximation coupled with a second-order time discretization. This method is based on a modification of the algorithm proposed by Goda [9] for finite element approximations. The main weakness of the Goda’s method lies in the fact that the normal pressure gradient on the boundary is held at its initial value. The MPM proposed in this paper allows to overcome this drawback by computing a preliminary pressure which satisfies to a Poisson problem derived from the Navier–Stokes equations. A Neumann boundary condition, similar to the one proposed by Karniadakis et al. [18], is used with an Adams–Bashforth scheme for the approximation of the diffusion term.

The results for an exact steady solution clearly show the weakness of the GPM, due to the incorrect treatment of the normal pressure gradient on the boundary. The space accuracy of the GPM strongly depends on the difference between the initial and the exact pressure gradients, and, therefore, it depends on the initial condition used for the velocity. Moreover, even for small values of this difference (about 10^{-3}), the machine accuracy is never reached for any variable. On the other hand, for the MPM, the errors on the velocity components and on the pressure decay exponentially when increasing the resolution and they regularly reach the machine accuracy when the polynomial degrees are sufficiently high. We noted also that, although the incompressibility constraint is not prescribed on the boundary, the discrete norm of the velocity divergence reaches the machine accuracy for the solution computed with the MPM. For the GPM, the velocity divergence on the boundary strongly depends on the difference between the initial and the exact pressure gradients and it remains quite large whatever the resolution is.

The results for a time-dependent exact solution with an unsteady pressure gradient on the boundary bring to the fore the inability of the GPM to correctly treat this type of solutions. The errors on the velocity and on the pressure exhibit a saturation due to the error in space induced by the incorrect treatment of the normal pressure gradient on the boundary. On the other hand, the results for the MPM confirm the second-order accuracy for each variable. Moreover, the introduction of the preliminary pressure reduces the slip velocity by one order of magnitude compared with the GPM.

The MPM has been applied successfully to the computation of complex instability phenomena in a rotating cavity with a superposed radial outflow and in a rotor–stator cavity. Axisymmetric annular and three-dimensional spiral structures, similar to the ones observed in the experiments, have been obtained. In addition, it must be noted that the MPM has been also extended to three-dimensional cylindrical configurations containing the rotation axis [29] and it has been applied successfully to the computation of instabilities and vortex breakdown in cylindrical rotor–stator cavities.

Acknowledgements

The computations were carried out on the Cray C98 of the C.N.R.S. computing center I.D.R.I.S. The research was made with supports from the “Direction Générale de l’Armement” (PhD grant for E.S.), from the C.N.R.S./D.F.G program “Numerical Flow Simulation” and from

PICASSO and Royal Society C.N.R.S. cooperative programs. The authors want to acknowledge gratefully Dr. Roger Peyret (University of Nice) for fruitful discussions.

References

- [1] Batoul A, Khallouf H, Labrosse G. Une méthode de résolution directe (pseudo-spectrale) du problème de Stokes 2D/3D instationnaire. Application à la cavité entraînée carrée. C R Acad Sciences Paris série II 1994;319:1455–61.
- [2] Botella O. On the solution of the Navier–Stokes equations using Chebyshev projection schemes with third order accuracy in time. *Comput Fluids* 1997;26:107–16.
- [3] Caldwell DR, Van Atta CW. Characteristics of Ekman boundary layer instabilities. *J Fluid Mech* 1970;44:79–95.
- [4] Chorin J. Numerical solution of the Navier–Stokes equations. *Math Comp* 1968;22:745–62.
- [5] Faller AJ, Kaylor RE. Investigations of stability and transition in rotating boundary layers. *Dyn Fluids Plasmas* 1966:309–29.
- [6] Faller AJ. Instability and transition of the disturbed flow over a rotating disc. *J Fluid Mech* 1991;230:245–69.
- [7] Fortin M, Peyret R, Temam R. Résolution numérique des équations de Navier–Stokes pour un fluide incompressible. *J de Mécanique* 1971;10(3):357–90.
- [8] Gauthier P, Gondret P, Rabaud M. Axisymmetric propagating vortices in the flow between a stationary and a rotating disk enclosed by a cylinder. *J Fluid Mech* 1999;386:105–27.
- [9] Goda K. A multistep technique with implicit difference schemes for calculating two or three dimensional cavity flows. *J Comp Phys* 1979;30:76–95.
- [10] Gottlieb D, Orszag SA. Numerical analysis of spectral methods: theory and application SIAM Monograph, vol. 26. Philadelphia, PA: SIAM; 1977.
- [12] Gresho PM, Sani RL. On the pressure boundary conditions for the incompressible Navier–Stokes equations. *Int J Numer Meth Fluids* 1987;7:1111–45.
- [13] Greenspan HP. The theory of rotating fluids. Cambridge, MA: Cambridge University Press; 1969.
- [14] Heinrichs W. Splitting techniques for the unsteady Stokes equations. *SIAM J Numer Anal* 1998;35(4):1646–62.
- [15] Hide R. On source–sink flows stratified in a rotating annulus. *J Fluid Mech* 1968;32:737–64.
- [16] Hugues S. Développement d’un algorithme de projection pour méthodes pseudospectrales: application à la simulation d’instabilités tridimensionnelles dans les cavités tournantes. Modélisation d’écoulements turbulents dans les systèmes rotor–stator. PhD thesis, Université d’Aix–Marseille II, 1998.
- [17] Hugues S, Randriamampianina A. An improved projection scheme applied to pseudospectral methods for the incompressible Navier–Stokes equations. *Int J Num Meth Fluids* 1998;28:501–21.
- [18] Karniadakis GE, Israeli M, Orszag SA. High order splitting methods for the incompressible Navier–Stokes equations. *J Comp Phys* 1991;97:414–43.
- [19] Kim J, Moin P. Application of a fractional step method to incompressible Navier–Stokes equations. *J Comp Phys* 1985;59:308–23.
- [20] Lilly DK. On the instability of Ekman boundary flow. *J Atmos Sci* 1966;23:481–90.
- [21] Orszag SA, Israeli M, Deville MO. Boundary conditions for incompressible flows. *J Sci Comp* 1986;1:75–111.
- [22] Pracht WE. *J Comp Phys* 1971;7:46–60.
- [23] Raspo I. Méthodes spectrales et de décomposition de domaine pour les écoulements complexes confinés en rotation. PhD thesis, Université d’Aix–Marseille II, 1996.
- [25] Savas O. Stability of Bödewadt flow. *J Fluid Mech* 1987;183:77–94.
- [26] Schouveiler L, Le Gal P, Chauve MP, Takeda Y. Spiral and circular waves in the flow between a rotating and a stationary disk. *Exp Fluids* 1999;26:179–87.
- [27] Serre E, Hugues S, Crespo del Arco E, Randriamampianina A, Bontoux P. Spiral and circular instability patterns in an Ekman boundary layer flow. *Int J Heat Fluid Flow* 2001;22:82–93.
- [28] Serre E, Crespo del Arco E, Bontoux P. Annular and spiral patterns in flows between rotating and stationary disks. *J Fluid Mech* 2001;434:65–100.
- [29] Serre E, Pulicani JP. A 3D pseudospectral method for convection in a rotating cylinder. *Comput Fluids* 2001;30:491–519.

- [30] Shen J. Hopf bifurcation of the unsteady regularized driven cavity flow. *J Comp Phys* 1991;95:228–45.
- [31] Sirivat A. Stability experiment of flow between a stationary and rotating disk. *Phys Fluids* 1991;3(11):2664–71.
- [32] Strikwerda JC, Lee YS. The accuracy of the fractional step method. *SIAM J Numer Anal* 1999;37:37–47.
- [33] Temam R. Sur l'approximation de la solution des équations de Navier–Stokes par la méthode des pas fractionnaires (I). *Arch Rat Mech Anal* 1969;32:135–53.
- [34] Vanel JM, Peyret R, Bontoux P. A pseudospectral solution of vorticity-stream function equations using the influence matrix technique. In: Morton KW, Baines MJ, editors. *Numerical methods for fluid dynamics II*, 1986. p. 463–75.
- [35] Van Kan J. A second order accurate pressure correction scheme for viscous incompressible flows. *SIAM J Sci Stat Comp* 1984;7:870–91.